Investigation of the role of surface lattice oxygen and bulk lattice oxygen migration of cerium-based oxygen carriers: XPS and designed H$_2$-TPR characterization

Dingkai Chen[a], Dedong He[a], Jichang Lu[a], Liping Zhong[a], Feng Liu[a], Jiangping Liu[a], Jie Yu[a], Gengping Wan[a,b], Sufang He[c], Yongming Luo[a,*]

[a] Faculty of Environmental Science and Engineering, Kunming University of Science and Technology, Kunming 650500, PR China
[b] Research Center for Analysis and Measurement, Hainan University, Haikou 570228, PR China
[c] Research Center for Analysis and Measurement, Kunming University of Science and Technology, Kunming 650093, PR China

ABSTRACT

The relationship between the oxygen species of cerium-based oxygen carriers and catalytic behavior, namely the correlation between catalytic activity and surface lattice oxygen (O_{S-L}) and that between catalytic stability and bulk lattice oxygen (O_{B-L}), was investigated by using CH$_3$SH and Ce$_{1-x}$Y$_x$O$_{2-\delta}$ (x = 0, 0.25, 0.50, 0.75, and 1.0) solid solutions as examples. Activity and stability experimental studies with corresponding XPS were performed to assess the role of definite surface oxygen in cerium-based oxygen carriers. The surface lattice oxygen (O_{S-L}), rather than the surface adsorbed oxygen (O_{S-A}), was observed to be responsible for the catalytic decomposition of CH$_3$SH. Further, the difference in catalytic activity between CeO$_2$ and Y-doped samples is closely associated with the insertion of Y^{3+} ion into the lattice of CeO$_2$ leading to the loss of surface lattice oxygen (O_{S-L}). H$_2$-temperature programmed reduction (TPR), a specially designed H$_2$-TPR, X-ray photoelectron spectroscopy, reaction product (CO and CO$_2$) analysis, and oxygen storage capacity tests were performed to demonstrate the migration of bulk lattice oxygen, which was directly related to the catalytic stability of CeO$_2$ and Y-doped catalysts. Direct evidences of the migration of bulk lattice oxygen over cerium-based oxygen carriers were obtained. Additionally, the migration rate of bulk lattice oxygen (O_{B-L}) within Ce$_{0.75}$Y$_{0.25}$O$_{2-\delta}$ was faster compared to the migration rate of bulk lattice oxygen (O_{B-L}) of CeO$_2$. Finally, improvements in catalytic stability are closely associated with the fact that bulk lattice oxygen (O_{B-L}) participates in the decomposition of CH$_3$SH through its faster migration to replenish surface lattice oxygen (O_{S-L}). The factors that influenced the migration rate of bulk lattice oxygen (O_{B-L}) were thus also subsequently investigated and discussed.

1. Introduction

Cerium oxide, or ceria, is one of the most industrially appealing oxides due to its outstanding oxygen storage and release capabilities achieved via the circular switch of the Ce^{4+}/Ce^{3+} redox couple [1]. Cerium-based materials have been increasingly investigated for their application in three-way catalysis [2,3], steam and dry reforming of hydrocarbons[4,5], solid oxide fuel cells [6], catalytic oxidation of volatile organic compounds [7–9], water–gas shift reaction in low temperatures [10,11], and as important oxygen carriers for chemical looping processes [12–16].

Chemical looping is one of several novel techniques employed to produce syngas with an ideal hydrogen to carbon (2:1) ratio together with high-purity hydrogen, as well as to effectively capture CO$_2$, thus proving beneficial for a series of problems related to the consumption of fossil fuels and global climate change [17–23]. Chemical-looping technology may be used for CO$_2$ capture during the combustion process, thus inhibiting the dilution of the corresponding reaction products with N$_2$. Accordingly, the high costs involved in gas separation would be spared since direct contact between fuel and air would be completely avoided [19,20]. The principle and process of chemical-looping reforming together with hydrogen production are similar to those of chemical-looping combustion. Therefore, the corresponding products, namely ideal syngas and high-purity hydrogen, can be obtained directly without

Table 1
Relative contents of Y, surface lattice oxygen (O_{S-L}) and Ce^{3+} within $Ce_{1-x}Y_xO_{2-\delta}$ samples (x = 0, 0.25, 0.50 and 0.75).

Samples	Relative content of Y (%) [a]	Relative content of O_{S-L} (%)[b]	Relative content of Ce^{3+} (%)[c]
CeO_2	0	100	6.1
$Ce_{0.75}Y_{0.25}O_{2-\delta}$	24.4%	91.82	5.5
$Ce_{0.50}Y_{0.50}O_{2-\delta}$	52.6%	84.70	5.3
$Ce_{0.25}Y_{0.75}O_{2-\delta}$	76.2%	60.50	5.8
Y_2O_3	100.0%	_ [d]	_ [d]

[a] The relative content of Y was calculated according to the ratio of the total area of $Ce_{1-x}Y_xO_{2-\delta}$ (x = 0, 0.25, 0.50 and 0.75) to the total area of Y_2O_3 based on Y3d XPS, and the total area of the sample was calculated according to the following equation: $A_Y = A(Y3d_{5/2}) + A(Y3d_{3/2})$ via a CasaXPS processing program.
[b] The relative content of surface lattice oxygen (O_{S-L}) was calculated according to the ratio of O_{S-L} area of $Ce_{1-x}Y_xO_{2-\delta}$ (x = 0.25, 0.50 and 0.75) to O_{S-L} area of CeO_2, and the O_{S-L} relative content of CeO_2 was designated to 100%.
[c] The relative content of Ce^{3+} was calculated according to the equations of (5), (6) and (7) based on Ce 3d spectra of $Ce_{1-x}Y_xO_{2-\delta}$ (x = 0, 0.25, 0.50 and 0.75).
[d] The data does not exist.

the high cost and substantial energy required for gas separation [17,22].

Regardless of whether chemical-looping combustion or reforming are being performed, oxygen transportation between the two reaction types (oxidation and reduction) is achieved by an oxygen carrier. In other words, oxygen transport during chemical-looping processes is generally performed via the periodic reduction/oxidation cycle between metal oxides and metal as well as the cycle between metal oxides with high valence and those with low valence [24,25]. A perfect example can be found in chemical-looping reforming accompanied by hydrogen production using a CeO_2 oxygen carrier. The release and replenishing of oxygen during the chemical-looping process focuses mostly on the redox cycle of the CeO_2/Ce_2O_3 system [26–29], composed of the following two steps:

$$2CeO_2(s) \rightarrow Ce_2O_3(s) + 1/2O_2(g) \tag{1}$$

$$Ce_2O_3(s) + H_2O(g) \rightarrow 2CeO_2(s) + H_2(g) \tag{2}$$
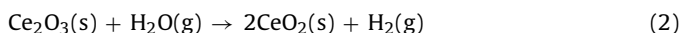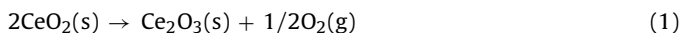
Recently, several studies have focused on chemical-looping processes using cerium-based materials as oxygen carriers, including CeO_2 and Fe-, Ni-, Zr-, and Y-modified CeO_2 [12–16]. These studies have mainly highlighted improvements in the reaction and redox properties of oxygen carriers. Moreover, some studies have reported that both surface oxygen and bulk oxygen species of oxygen carriers participate in the processes of CH_4 chemical looping and indirectly demonstrated the migration of bulk oxygen species via kinetic and pulse technique [30–34]. However, the detailed roles of the oxygen species (surface adsorbed oxygen, surface lattice oxygen, and bulk lattice oxygen) within oxygen carriers have not yet been clearly elucidated. In other words, the interrelationship between oxygen species and catalytic behavior (activity and stability) are not well understood. Nevertheless, understanding the roles of oxygen species within oxygen carriers is of practical importance in the design and development of high-performance oxygen carriers for chemical-looping processes.

Since the fuel reactor usually runs at relatively high temperatures during chemical-looping processes (above 800 °C) [35,36], the use of hydrocarbons (such as CH_4) as model reactants to estimate the role of oxygen species within oxygen carriers of cerium-based materials at high-temperature is impractical. In order to investigate the role of oxygen species, the choice of a suitable model reactant is of particular importance. Methyl mercaptan (CH_3SH) is an organic sulfur compound present in natural gas. Based on environmental protection laws and industrial applications, the total sulfur content of natural gas must be kept below 5 ppmv [37]. Therefore, the removal of CH_3SH and other sulfur-containing compounds has attracted widespread attention [38–43]. In our previous work [44–47], it was found that CH_3SH can be completely converted at 450 °C over nanosized ceria-based catalysts; however, the role of oxygen species over these ceria-based materials as well as the deactivation mechanism for CH_3SH catalytic decomposition remained

poorly understood. More importantly, the temperature (450 °C) of complete decomposition of CH_3SH over ceria-based catalysts was consistent with the reduction temperature of ceria surface oxygen species and far lower than that of bulk lattice oxygen, proving beneficial in the design of experiments to demonstrate the roles of the various oxygen species. Therefore, based on these results, it can be deduced that CH_3SH is a suitable model reactant.

Generally, cerium-based oxygen carriers possess three types of oxygen species, namely surface adsorbed oxygen (O_{S-A}), surface lattice oxygen (O_{S-L}), and bulk lattice oxygen (O_{B-L}). A series of yttrium-doped cerium-based carrier ($Ce_{1-x}Y_xO_{2-\delta}$; x = 0, 0.25, 0.50, 0.75, and 1.0) solid solutions were prepared and characterized to investigate the roles of the oxygen species within them using CH_3SH as a model reactant. The present study aims to understand the interrelationship between oxygen species and catalytic behavior by assessing the correlation between catalytic activity and O_{S-L} as well as that between catalytic stability and O_{B-L}. In addition, the factors affecting the migration rate of O_{B-L} were investigated and discussed.

2. Experimental

2.1. Preparation of $Ce_{1-x}Y_xO_{2-\delta}$ solid solution

$Ce(NO_3)_3 \cdot 6H_2O$ and $Y(NO_3)_3 \cdot 6H_2O$ were used as precursors and citric acid was used as a ligand to synthesize $Ce_{1-x}Y_xO_{2-\delta}$ catalyst samples via a citrate-complexation route with the aid of microwave radiation. The general procedures are described below. The calculated amounts of $Ce(NO_3)_3 \cdot 6H_2O$, $Y(NO_3)_3 \cdot 6H_2O$, and citric acid were dissolved in deionized water stirred at 60 °C for 5 min to yield a homogenous and transparent mixture solution. The solution was then calcined in a microwave muffle furnace (CEM Corporation in USA, phoenix standard unit) at 500 °C for 2 h to obtain the $Ce_{1-x}Y_xO_{2-\delta}$ (x = 0, 0.25, 0.50, 0.75, and 1.0) catalyst samples.

2.2. Characterization of $Ce_{1-x}Y_xO_{2-\delta}$ solid solution

2.2.1. X-ray diffraction (XRD) analysis

XRD patterns were recorded on a X-ray powder diffractometer (Rigaku D/max-1200) with Cu Kα irradiation, at 40 kV and 30 mA. All the samples were scanned in the 2θ range between 20° and 80° with a step size of 0.02°. The particle size was calculated based on the width of the main diffraction peak as assessed with the MDI Jade 5.0 software using the Scherrer equation. The lattice parameter 'a' was calculated using the most prominent peak (111) according to the following formulas [48]:

$$a = d\sqrt{h^2 + k^2 + l^2} \tag{3}$$

$$d = \frac{\lambda}{2\sin\theta} \tag{4}$$

Where d represents the inter-planar spacing and θ represents the diffraction angle of the (111) plane.

2.2.2. Brunauer-Emmett-Teller (BET) surface area measurement

Surface area and pore volume were determined by N_2 adsorption isotherms at $-196\,°C$ with a NOVA 4200e instrument. All the catalyst samples were degassed at $250\,°C$ for 2 h under high vacuum before measurement. BET specific surface area was calculated by the BET method according to the data of adsorption branch in the relative pressure range from 0.05 to 0.25.

2.2.3. Raman

Raman spectra were recorded on a Renishaw Raman spectrometer at room temperature with a 514 nm emission line from an Ar^+ laser.

2.2.4. X-ray photoelectron spectroscopy (XPS)

XPS was performed using a PHI 5000 Versa Probe II spectrometer with monochromatic Al-Kα excitation, and C1s at 284.6 eV was applied to account for charging effects. A CasaXPS processing program was used for background subtraction and peak fitting.

2.2.5. H_2 temperature-programmed reduction (H_2-TPR)

The mobility and redox properties of catalyst samples were evaluated via H_2-TPR measurement using hydrogen (H_2) as a reductant. Briefly, 50 mg of catalyst samples were loaded in a quartz reactor and pretreated with a gas mixture (5 vol% O_2 in Ar) at $400\,°C$ for 1 h. The pretreated sample was then cooled to $100\,°C$ in the flow of ultra-pure Ar, following which the sample was heated to $900\,°C$ under the mixed gas flow (10 vol% H_2 in Ar) at a heating rate of $10\,°C\,min^{-1}$. H_2 consumption was measured using an online thermal conductivity detector (TCD).

2.2.6. Designed H_2-TPR experiments

Two types of designed H_2-TPR experiments were employed to demonstrate the migration of bulk lattice oxygen and the consumption of surface oxygen, respectively.

In the first designed H_2-TPR experiment, 50 mg of CeO_2 were used for each test. The CeO_2 sample was pretreated and cooled as described in the above H_2-TPR section. The pretreated and cooled sample was heated to $600\,°C$ at a heating rate of $10\,°C\,min^{-1}$ and kept at $600\,°C$ for various time periods (1, 3, 5, 10, 15, and 20 h) under a 10 vol% H_2/Ar gas flow. Finally, the resulting sample was further heated to $950\,°C$ under a 10 vol% H_2/Ar gas flow at a heating rate of $10\,°C\,min^{-1}$. The corresponding H_2 consumption was measured using an online TCD.

In the second designed H_2-TPR experiment, 50 mg of catalyst samples ($Ce_{0.75}Y_{0.25}O_{2-\delta}$ or CeO_2) were pretreated and cooled as described in the above H_2-TPR section. The pretreated and cooled samples were then heated to $450\,°C$ at a heating rate of $10\,°C\,min^{-1}$ and maintained at $450\,°C$ for 1 or 2 h under a 10 vol% H_2/Ar gas flow. Subsequently, the resulting samples were cooled to $100\,°C$ under an ultra-pure Ar gas flow. Finally, the cooled samples ($Ce_{0.75}Y_{0.25}O_{2-\delta}$ and CeO_2) were reheated at a heating rate of $10\,°C\,min^{-1}$ under a 10 vol% H_2/Ar gas flow to $850\,°C$ and $950\,°C$, respectively. The corresponding H_2 consumption was measured using an online TCD.

2.2.7. Oxygen storage capacity (OSC)

The OSC of CeO_2 and $Ce_{0.75}Y_{0.25}O_{2-\delta}$ samples was assessed by CO pulse injection using a micro-reactor system. Prior to measurement, 50 mg of the samples were firstly purged in flow of 20 vol% O_2/He (30 mL min^{-1}) at $500\,°C$ for 1 h. Subsequently, the sample was cooled down to $450\,°C$ under an ultra-pure He flow. A CO gas (99.99%) pulse was introduced to the system at $450\,°C$ every 6 min using a six-way gas-sampling valve equipped with a measuring ring (50 μmol L^{-1}); 30 CO pulse sequences were performed for each sample.

2.3. Catalytic experiments

Catalytic activity decomposition of the model reactant (CH_3SH) was performed in a fixed-bed micro-reactor at atmospheric pressure. A 200-mg sample of each catalyst with a particle size between 40 and 60 mesh was used for each test, and the feed gas consisted of 1 vol% CH_3SH (balanced with N_2, 30 mL min^{-1}). The reactants and products were detected using two online gas chromatographs equipped with two flame ionization detectors, a flame photometric detector, and two TCDs.

The conversion of CH_3SH was calculated on the basis of the following equation:

$$CH_3SH\ Conversion = \frac{C_{[CH3SH]in} - C_{[CH3SH]out}}{C_{[CH3SH]in}} \times 100\%$$

Where $C_{[CH3SH]in}$ and $C_{[CH3SH]out}$ are the CH_3SH concentrations in the inlet and outlet, respectively.

3. Results and discussion

3.1. Structural characterization

3.1.1. XRD

XRD patterns of CeO_2, $Ce_{0.75}Y_{0.25}O_{2-\delta}$, $Ce_{0.5}Y_{0.5}O_{2-\delta}$, $Ce_{0.25}Y_{0.75}O_{2-\delta}$, and Y_2O_3 are presented in Fig. S1. No crystalline phase attributed to the Y_2O_3 species was observed in the patterns of $Ce_{0.75}Y_{0.25}O_{2-\delta}$, $Ce_{0.5}Y_{0.5}O_{2-\delta}$, and $Ce_{0.25}Y_{0.75}O_{2-\delta}$, likely due to the doping Y species (such as Y^{3+} ions) being effectively inserted into the CeO_2 lattice to form a homogeneous solid solution ($Ce_{1-x}Y_xO_{2-\delta}$) or the Y species being highly dispersed and therefore composed of very small crystals and/or presenting with an amorphous structure below the limits of detection of XRD [49,50]. As shown in Fig. S1 (inset), the diffraction peak of the (111) plane was shifted slightly towards a lower 2θ value with the increase in Y loading. This was due to an increase in the size of the fluorite unit cell with increasing Y^{3+} content since the radius of the Y^{3+} ion (1.03 Å) is larger than that of Ce^{4+} [51–53] (0.97 Å). Moreover, it is also noted that the diffraction peaks of $Ce_{1-x}Y_xO_{2-\delta}$ (x = 0.25, 0.50, and 0.75) samples became broader with a weaker relative intensity with the increase in Y loading. The changes in the XRD peak intensities and linewidths led to a decrease in the crystallite sizes of $Ce_{0.75}Y_{0.25}O_{2-\delta}$, $Ce_{0.5}Y_{0.5}O_{2-\delta}$, and $Ce_{0.25}Y_{0.75}O_{2-\delta}$ samples with respect to CeO_2.

Based on the results of XRD characterization, it can be concluded that the Y^{3+} cation was successfully inserted into the lattice of CeO_2. However, whether the isolated Y species actually formed very small crystals or an amorphous phase on the surface of $Ce_{1-x}Y_xO_{2-\delta}$ samples (x = 0.25, 0.50, and 0.75) was not determined through XRD.

3.1.2. XPS

XPS was used in order to confirm that the isolated Y species were inserted within the lattice and not on the surface of $Ce_{1-x}Y_xO_{2-\delta}$ samples (x = 0.25, 0.50, and 0.75). The Y 3d core-level XPS spectra of $Ce_{0.75}Y_{0.25}O_{2-\delta}$, $Ce_{0.50}Y_{0.50}O_{2-\delta}$, $Ce_{0.25}Y_{0.75}O_{2-\delta}$, and Y_2O_3 (Fig. S2) were deconvoluted into two peaks, originating from the contribution of two spin-orbit components, located at 156.7 eV and 158.8 eV and assigned to $Y3d_{5/2}$ and $Y3d_{3/2}$ [54] spin-orbit components, respectively. The intensities of the Y 3d peaks of the $Ce_{1-x}Y_xO_{2-\delta}$ (x = 0, 0.25, 0.50, 0.75, and 1.0) samples gradually increased with the loading of Y (Table 1). The calculated relative content of Y on the surface of $Ce_{0.75}Y_{0.25}O_{2-\delta}$, $Ce_{0.50}Y_{0.50}O_{2-\delta}$, and $Ce_{0.25}Y_{0.75}O_{2-\delta}$ was in close agreement with the theoretical calculation value (ratio)

(Table 1). These results, in combination with the above XRD results, indicate that all the Y species (Y^{3+} ions) were highly dispersed within the ceria samples to form homogeneous solid solutions.

Ce 3d core-level XPS spectra of the Ce$_{1-x}$Y$_x$O$_{2-\delta}$ samples (x = 0, 0.25, 0.50, and 0.75) (Fig. S3) show that all four samples (CeO$_2$, Ce$_{0.75}$Y$_{0.25}$O$_{2-\delta}$, Ce$_{0.5}$Y$_{0.5}$O$_{2-\delta}$, and Ce$_{0.25}$Y$_{0.75}$O$_{2-\delta}$) can be deconvoluted into eight peaks, corresponding to four pairs of spin-orbit doublets. Generally, the peaks marked as v (881.2 eV), v″ (887.3 eV), v‴ (897.1 eV), u (899.8 eV), u″ (906.1 eV), and u‴ (915.4 eV) arise from the contribution of Ce^{4+} species, while the peaks labeled as v′ (883.7 eV) and u′ (902.0 eV) originate from the contribution of Ce^{3+} species [55], thus indicating the coexistence of Ce^{3+} and Ce^{4+} within the four samples. According to the ratio of Ce^{3+} ion peak area to that of the total Ce^{3+} and Ce^{4+} ion peak area, the following equations were used to calculate the relative content of Ce^{3+} within the samples [56]:

$$A_{Ce(III)} = A_{v'} + A_{u'} \tag{5}$$

$$A_{Ce(IV)} = A_v + A_{v''} + A_{v'''} + A_u + A_{u''} + A_u{}''' \tag{6}$$

$$Relative\, content\, of\, Ce^{3+} = A_{Ce(III)} / \{A_{Ce(IV)} + A_{Ce(III)}\} \tag{7}$$

Where A$_x$ represents the area of peak x. The corresponding calculation results are tabulated in Table 1. There was a significant decrease in the area of both Ce^{4+} and Ce^{3+} with increasing Y loading, indicating that more Ce has been substituted by Y, thus resulting in the formation of more oxygen vacancies according to the charge compensation [57].

As illustrated in Fig. S4, there was a decline in the relative content of Ce^{3+} for the doped Ce$_{1-x}$Y$_x$O$_{2-\delta}$ samples with the increase in Y loading from 0 to 0.5, closely associated with the prior substitution of Ce^{3+} with Y^{3+} ion within the fluorite structure [54]. However, with further increases in the loading of Y up to 0.75, there was an increase in the relative content of Ce^{3+} over Ce$_{0.25}$Y$_{0.75}$O$_{2-\delta}$, assigned to the reduction of Ce^{4+} ion in the cubic structure Y$_2$O$_3$ lattice in order to maintain the electrostatic balance [54].

3.1.3. Raman

In general, Raman characterization is an effective technique to gain insight into the exact structure and formation of oxygen vacancy defects within cerium-based materials. Accordingly, CeO$_2$, Ce$_{0.75}$Y$_{0.25}$O$_{2-\delta}$, Ce$_{0.50}$Y$_{0.50}$O$_{2-\delta}$, and Ce$_{0.25}$Y$_{0.75}$O$_{2-\delta}$ were characterized by Raman spectroscopy (Fig. S5). An intense band centered at 465 cm^{-1} was observed in the spectrum of CeO$_2$, corresponding to the characteristic F$_{2g}$ vibration mode of O atoms surrounded by Ce^{4+} ion to form the Ce-O8 unit. The band around 465 cm^{-1} was clearly observed in the spectra of Ce$_{0.75}$Y$_{0.25}$O$_{2-\delta}$ and Ce$_{0.50}$Y$_{0.50}$O$_{2-\delta}$, thus implying that the original fluorite-type structure was retained for these two samples. However, compared with CeO$_2$, the corresponding intensities of Ce$_{0.75}$Y$_{0.25}$O$_{2-\delta}$ and Ce$_{0.50}$Y$_{0.50}$O$_{2-\delta}$ decreased considerably and their peaks position shifted, likely due to the insertion of metal species in ceria lattice [58]. The disappearance of the band (at 465 cm^{-1}) with further increases in the loading of Y may be due to the excessive incorporation of Y^{3+} into the lattice of CeO$_2$, which would lead to severe framework deformation and/or the collapse of the original fluorite-type structure for CeO$_2$ [59–61].

3.2. The role of surface lattice oxygen

Fig. 1 shows changes in the conversion of CH$_3$SH over CeO$_2$, Ce$_{0.75}$Y$_{0.25}$O$_{2-\delta}$, Ce$_{0.5}$Y$_{0.5}$O$_{2-\delta}$, and Ce$_{0.25}$Y$_{0.75}$O$_{2-\delta}$ with varying reaction temperature. When the reaction temperature was higher than 500 °C, no change was observed in the conversion of CH$_3$SH for the four catalyst samples. Within the reaction temperature region of 350–500 °C, the activity of Ce$_{0.75}$Y$_{0.25}$O$_{2-\delta}$
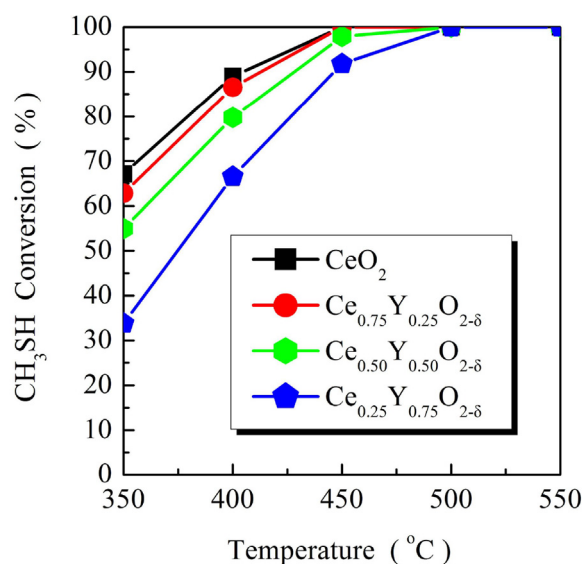

Fig. 1. CH$_3$SH conversion with reaction temperature over Ce$_{1-x}$Y$_x$O$_{2-\delta}$ samples (x = 0, 0.25, 0.5 and 0.75).
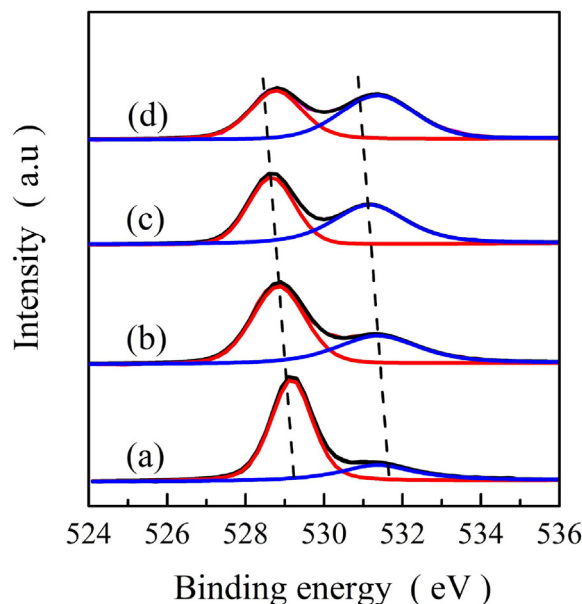

Fig. 2. O1s XP spectra of (a) CeO$_2$, (b) Ce$_{0.75}$Y$_{0.25}$O$_{2-\delta}$, (c) Ce$_{0.5}$Y$_{0.5}$O$_{2-\delta}$ and (d) Ce$_{0.25}$Y$_{0.75}$O$_{2-\delta}$.

was slightly lower or comparable to that of CeO$_2$, yet the CH$_3$SH conversions of Ce$_{0.5}$Y$_{0.5}$O$_{2-\delta}$ and Ce$_{0.25}$Y$_{0.75}$O$_{2-\delta}$ were far lower than those of CeO$_2$ and Ce$_{0.75}$Y$_{0.25}$O$_{2-\delta}$. Moreover, the activities of the three Y-doped samples were in the order of Ce$_{0.75}$Y$_{0.25}$O$_{2-\delta}$ > Ce$_{0.5}$Y$_{0.5}$O$_{2-\delta}$ > Ce$_{0.25}$Y$_{0.75}$O$_{2-\delta}$, indicating that the conversion of CH$_3$SH decreases with increasing Y loading.

In order to explore the underlying reasons for the activity difference among CeO$_2$ and the three Y-doped Ce$_{1-x}$Y$_x$O$_{2-\delta}$ samples (x = 0.25, 0.5, and 0.75), O1s core-level XPS spectra of CeO$_2$, Ce$_{0.75}$Y$_{0.25}$O$_{2-\delta}$, Ce$_{0.5}$Y$_{0.5}$O$_{2-\delta}$, and Ce$_{0.25}$Y$_{0.75}$O$_{2-\delta}$ were recorded (Fig. 2). Two peaks were detected for both CeO$_2$ and the three Y-doped Ce$_{1-x}$Y$_x$O$_{2-\delta}$ samples. The photoelectron peak with binding energy located at approximately 529 eV was ascribed to the surface lattice oxygen (O$_{S-L}$), whereas the second photoelectron at 531.5 eV was attributed to surface adsorbed oxygen (O$_{S-A}$) [62]. It is remarkable that the intensity of the O$_{S-L}$ peak decreased with increasing Y
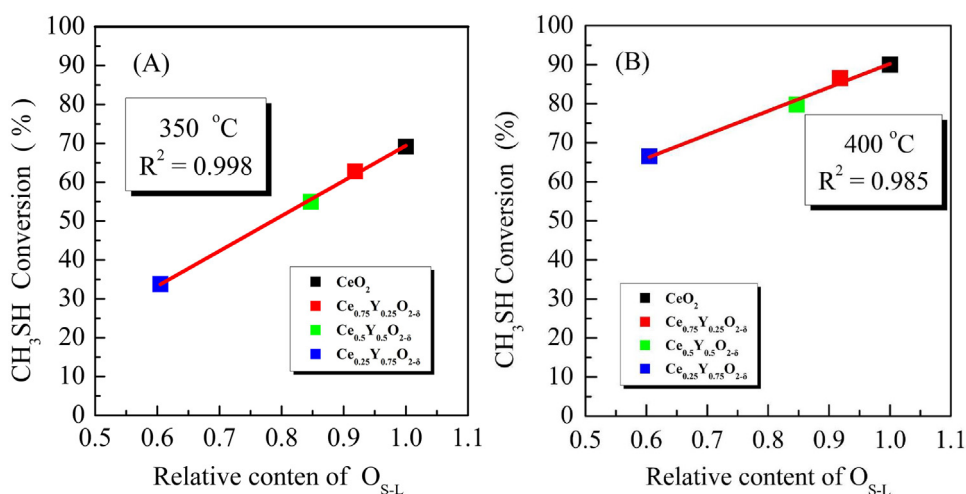
Fig. 3. The interrelation between surface lattice oxygen (O_{S-L}) and the conversion of CH_3SH over $Ce_{1-x}Y_xO_{2-\delta}$ samples (x = 0, 0.25, 0.5, and 0.75) under (A) 350 °C and (B) 400 °C.
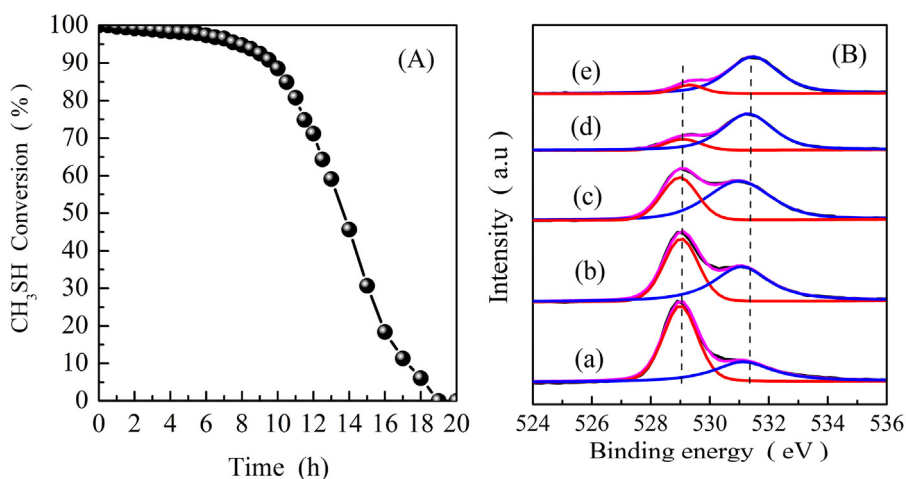

Fig. 4. (A) CH_3SH conversion under time-on-stream test at 450 °C over CeO_2 and (B) O1s XP spectra of CeO_2 and CeO_2 after time-on-stream test at 450 °C for various time: (a) fresh, (b) 1 h, (c) 2 h, (d) 10 h, (e) 20 h.

loading, whereas the intensity of O_{S-A} increased with increasing Y loading. The increase of O_{S-A} peak intensity can be due to the fact that the oxygen vacancies caused by the insertion of Y^{3+} cations can capture more carbonate and hydroxide species according to relevant literatures [63–,64,65]. The reduced O_{S-L} peak intensity indicates that O_{S-L} may play a role in the catalytic decomposition of CH_3SH.

In order to expound the interrelationship between O_{S-L} and the conversion of CH_3SH, the conversions of CH_3SH over CeO_2, $Ce_{0.75}Y_{0.25}O_{2-\delta}$, $Ce_{0.5}Y_{0.5}O_{2-\delta}$, and $Ce_{0.25}Y_{0.75}O_{2-\delta}$ as a function of the relative content of O_{S-L} at 350 °C and 400 °C are presented in Fig. 3, with the corresponding data being linearly fitted. A decrease in the conversion of CH_3SH with the decline in relative content of O_{S-L} was observed at both 350 °C and 400 °C. More importantly, the regression coefficient at the two reaction temperatures was approximately 0.99. Therefore, it can be deduced that O_{S-L} is responsible for the catalytic decomposition of CH_3SH.

To further confirm the role of O_{S-L} in the decomposition of CH_3SH over cerium-based materials, the conversion of CH_3SH in relation to reaction time over CeO_2 at 450 °C and the O1 s XPS spectra of CeO_2 and CeO_2 after time-on-stream test are shown in Fig. 4. The relative content of O_{S-L} of CeO_2 and CeO_2 after time-on-stream test are summarized in Table 2. The conversion of CH_3SH over CeO_2

Table 2
Relative contents of surface lattice oxygen (O_{S-L}) and Ce^{3+} within CeO_2 and CeO_2 after time-on-stream test for different time.

Samples	Relative content of O_{S-L} (%) [a]	Relative content of Ce^{3+} (%) [b]
CeO_2(0 h)[c]	100	6.1
CeO_2 (1 h)[c]	81	13.1
CeO_2 (2 h)[c]	53	29.9
CeO_2 (10 h)[c]	20	35.5
CeO_2 (20)[c]	13	51.0

[a] The relative content of surface lattice oxygen (O_{S-L}) was calculated according to O1 s spectra of CeO_2 and CeO_2 after time-on-stream test, and the O_{S-L} relative content of CeO_2 was assigned to 100%.

[b] The relative content of Ce^{3+} was calculated according to the equations of (5), (6) and (7) based on Ce 3d spectra of CeO_2 and CeO_2 after time-on-stream test.

[c] Reaction time of time-on-stream test in the brackets, and spent CeO_2 after time-on-stream test for 20 h.

was observed to gradually decrease with reaction time as did the O_{S-L} of the catalyst. After the 20-h time-on-stream test, the CeO_2 catalyst was completely deactivated and the O_{S-L} was practically consumed. However, there was an slightly increase in O_{S-A} during the time-on-stream test, which could be attributed to the formation of more oxygen vacancies because of the loss of surface lattice oxygen as reaction duration increased. The oxygen vacancies could
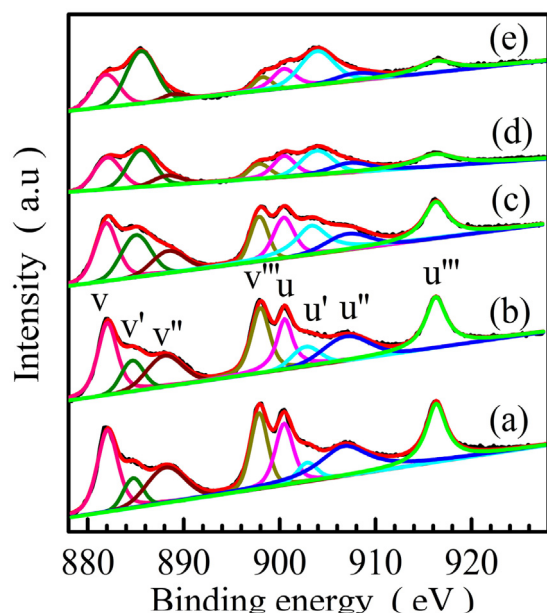
Fig. 5. Ce 3d XP spectra of CeO_2 and CeO_2 after time-on-stream test at 450 °C for various time: (a) 0, (b) 1 h, (c) 2 h, (d) 10 h, (e) 20 h.

Fig. 6. CH_3SH conversion as a function of reaction time under 450 °C over $Ce_{1-x}Y_xO_{2-\delta}$ (x = 0, 0.25, 0.50 and 0.75).

capture carbonate and hydroxide species originated from reaction products (such as CO and CO_2 etc.), which was responsible for the slight increase of this O_{S-A} [63–65]. The results further and directly manifest that the O_{S-L} plays a dominant role in determining the decomposition of CH_3SH.

The correlation between O_{S-L} and CH_3SH catalytic decomposition was further demonstrated with Ce 3d XPS spectra of CeO_2 and CeO_2 after the time-on-stream test over various time periods (Fig. 5); the corresponding relative contents are summarized in Table 2. Compared with fresh CeO_2, six photoelectron peaks, assigned to the contribution of Ce^{4+} species, decreased with the increase in the time on the stream, whereas the two photoelectron peaks attributed to the contributions of Ce^{3+} species increased with the increase in reaction time, likely due to the large amount of Ce^{4+} species being reduced to Ce^{3+} species during the time-on-stream test. In general, the switch from Ce^{4+} to Ce^{3+} is accompanied with release of lattice oxygen [66], and therefore O_{S-L} is involved in the process of CH_3SH catalytic decomposition.

According to the results obtained from the above experiments and characterization, two conclusions can be conceivably deduced. First, O_{S-L}, rather than O_{S-A}, is responsible for the catalytic decomposition of CH_3SH. Second, the difference in catalytic activity between CeO_2 and the three Y-doped samples ($Ce_{0.75}Y_{0.25}O_{2-\delta}$, $Ce_{0.5}Y_{0.5}O_{2-\delta}$, and $Ce_{0.25}Y_{0.75}O_{2-\delta}$) is associated with the insertion of Y^{3+} ion into the lattice of CeO_2 causing the loss of O_{S-L} in order to maintain electric neutrality [67]. The greater the number of Y^{3+} ions incorporated into the CeO_2 lattice, the greater the O_{S-L} loss, thus resulting in a decrease in catalytic activity.

3.3. Bulk lattice oxygen migration

The conversions of CH_3SH with reaction time at 450 °C over CeO_2 and the doped catalyst samples ($Ce_{0.75}Y_{0.25}O_{2-\delta}$, $Ce_{0.5}Y_{0.5}O_{2-\delta}$, and $Ce_{0.75}Y_{0.25}O_{2-\delta}$) are shown in Fig. 6. Compared with CeO_2, it is interesting that the rapid deactivation is only observed for $Ce_{0.25}Y_{0.75}O_{2-\delta}$, but not for $Ce_{0.75}Y_{0.25}O_{2-\delta}$ and $Ce_{0.5}Y_{0.5}O_{2-\delta}$. Based on the results obtained from section 3.2, namely that O_{S-L} plays a particularly important role in determining the decomposition of CH_3SH and that the relative content of O_{S-L} of CeO_2 is higher than in the three doped catalyst samples ($Ce_{0.75}Y_{0.25}O_{2-\delta}$, $Ce_{0.50}Y_{0.50}O_{2-\delta}$,
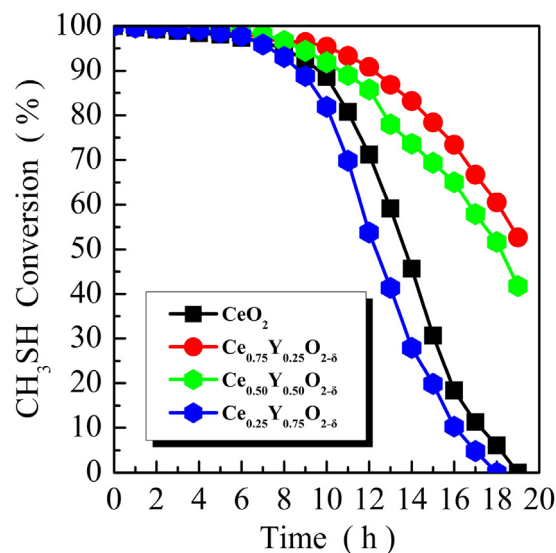
and $Ce_{0.25}Y_{0.75}O_{2-\delta}$), which would be responsible for its the highest catalytic activity. Furthermore, it was demonstrated that O_{S-A} is not involved in the decomposition of CH_3SH. Herein, the observed improvements in catalytic stability of $Ce_{0.75}Y_{0.25}O_{2-\delta}$ and $Ce_{0.5}Y_{0.5}O_{2-\delta}$ cannot be well explained simply according to O_{S-L} and O_{S-A}. Therefore, we speculate that the improvement in catalytic stability is closely associated with the fact that O_{B-L} participates in the decomposition of CH_3SH through its migration to replenish O_{S-L}.

In order to confirm the above assumption and directly demonstrate the migration of O_{B-L}, and therefore to explain the differences in catalytic stability between CeO_2 and the Y-doped samples, H_2-TPR, designed H_2-TPR, XPS, reaction products (CO and CO_2) analysis, and OSC were employed to compare and characterize CeO_2 and the doped samples.

3.3.1. H_2-TPR

H_2-TPR is usually performed to characterize the redox properties of materials. The corresponding H_2-TPR profiles of CeO_2, $Ce_{0.75}Y_{0.25}O_{2-\delta}$, $Ce_{0.50}Y_{0.50}O_{2-\delta}$, and $Ce_{0.25}Y_{0.75}O_{2-\delta}$ are shown in Fig. S6. Two H_2 consumption peaks, centered at approximately 500 °C and 800 °C, were detected for CeO_2; these peaks are characteristic of the reduction of surface oxygen species and bulk oxygen species [68], respectively. Only one broad H_2 consumption peak, attributed to the co-reduction of surface and bulk lattice oxygen species [69], was detected for the three doped samples at the temperature range 450–650 °C, which might be related to the substitution of Ce^{4+} ion with Y^{3+} not only effectively inhibiting the growth of crystal size but also reducing the activation energy for the diffusion of the oxygen ion within the lattice [70], thus improving the mobility of oxygen as well as promoting the migration of O_{B-L} to replenish surface oxygen. Moreover, it was found that the corresponding reduction peak of the doped samples gradually shifted to higher temperature with the increase in Y loading, attributed to the synergistic effect of the lattice distortion (or collapse) and the decreasing reduction degree of materials [62]. Herein, through the comparison of CeO_2 with the doped samples, H_2-TPR characterization provides indirect proof of the migration of O_{B-L}.
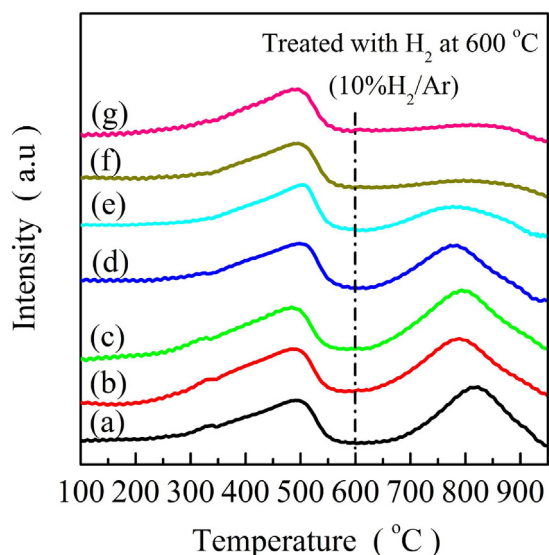
3.3.2. Designed H_2-TPR

In order to directly demonstrate the migration of O_{B-L} and understand the difference in catalytic stability between CeO_2 and

Table 3

H_2 consumption amount, migration and migration rate of bulk lattice oxygen (O_{B-L}) within CeO_2 and CeO_2 treated with 10% H_2/Ar at 600 °C for different time.

Samples	H_2 consumption (μmol/g) [a]	Migration amount of O_{B-L} (μmol/g) [b]	Migration rate of O_{B-L} (μmol/g s) [c]
Untreated CeO_2	645	0	0
Treated CeO_2 (1 h) [d]	643	1.0	0.0003
Treated CeO_2 (3 h) [d]	641	2.0	0.0003
Treated CeO_2 (5 h) [d]	426	109.5	0.0061
Treated CeO_2 (10 h) [d]	307	169.0	0.0047
Treated CeO_2 (15 h) [d]	87	279.0	0.0052
Treated CeO_2 (20 h) [d]	55	295.0	0.0041

[a] H_2 consumption of bulk lattices oxygen (O_{B-L}) was calculated according to TPR profiles at temperature range of 650–950 °C.

[b] The migration amount of bulk lattices oxygen (O_{B-L}) = (645- H_2 consumption of treated CeO_2)/2.

[c] The migration rate of bulk lattices oxygen (O_{B-L}) = The migration amount of (O_{B-L})/treated time.

[d] CeO_2 was treated at 600 °C with 10% H_2/Ar, the corresponding treated time in brackets.

Table 4

H_2 consumption of surface and bulk lattice oxygen of CeO_2 and $Ce_{0.75}Y_{0.25}O_{2-\delta}$ treated with 10% H_2/Ar at 450 °C for different time.

Sample	H_2 consumption (μmol/g) [a]	H_2 consumption (μmol/g) [b]	O_{S-L} consumption (μmol/g) [c]	O_{B-L} migration (μmol/g) [d]	O_{S-L} consump rate (μmol/g^{-1} s^{-1} [e])	O_{B-L} migration rate (μmol/g^{-1} s^{-1}) [f]
Untreated CeO_2	549	645	0	0	0	0
Treated CeO_2 (1 h [g]	276	645	136.5	0	0.0379	0
Treated CeO_2 (2 h [g]	12	645	268.5	0	0.0373	0
Untreated $Ce_{0.75}Y_{0.25}O_{2-\delta}$	539	– [e]	0	0	0	0
Treated $Ce_{0.75}Y_{0.25}O_{2-\delta}$(1 h [g]	366	– [e]	86.5	50.0	0.0379	0.0139
Treated $Ce_{0.75}Y_{0.25}O_{2-\delta}$(1 h [g]	192	– [e]	173.5	95.0	0.0373	0.0132

[a] H_2 consumption of surface lattice oxygen (O_{S-L}) was calculated according to TPR profiles at temperature range of 300–600 °C.

[b] H_2 consumption of bulk lattices oxygen (O_{B-L}) was calculated according to TPR profiles at temperature range of 650–950 °C.

[c] O_{S-L} consumption of CeO_2 = (549- H_2 consumption of O_{S-L})/2, and O_{S-L} consumption of $Ce_{0.75}Y_{0.25}O_{2-\delta}$ = (539- H_2 consumption of O_{S-L})/2.

[d] O_{B-L} migration amount of CeO_2 = (645- H_2 consumption of O_{S-L})/2, and O_{B-L} migration amount of $Ce_{0.75}Y_{0.25}O_{2-\delta}$ = O_{S-L} consumption of CeO_2— O_{S-L} consumption of $Ce_{0.75}Y_{0.25}O_{2-\delta}$.

[e] Assumed that CeO_2 and $Ce_{0.75}Y_{0.25}O_{2-\delta}$ have the same H_2 consumption rates under the same conditions.

[f] The migration rate of bulk lattices oxygen (O_{B-L}) = The migration amount of (O_{B-L})/treated time.

[g] CeO_2 and $Ce_{0.75}Y_{0.25}O_{2-\delta}$ were treated at 450 °C with 10% H_2/Ar, and the corresponding treated time in brackets.

Fig. 7. Designed H_2-TPR profiles of CeO_2 and CeO_2 treated with 10% H_2/Ar at 600 °C for different time: (a) 0 h, (b) 1 h, (c) 3 h, (d) 5 h, (e) 10 h, (f) 15 h and (g) 20 h.

the doped $Ce_{1-x}Y_xO_{2-\delta}$ samples, two designed H_2-TPR experiments were performed.

Fig. 7 provides the designed H_2-TPR profiles of CeO_2 and CeO_2 treated with 10 vol% H_2/Ar at 600 °C for different time periods. The corresponding H_2 consumptions of O_{B-L} are summarized in Table 3. When the CeO_2 sample was treated (at 600 °C with 10 vol% H_2/Ar) for no more than 3 h, the hydrogen consumption amount of O_{B-L} was maintained relatively stable (about 640 μmol/g) but the reduction peak slightly shifted to a lower temperature. When

the treatment time increased from 3 to 10 h, a decrease in H_2 consumption amount (from 640 to 300 μmol/g) as well as a shift in the reduction peak towards a lower temperature were observed. With a further increase in treatment time, the reduction peak of O_{B-L} gradually disappeared, with the corresponding H_2 consumption amounts of the CeO_2 sample treated for 15 and 20 h being 87 and 55 μmol/g, respectively, thus indicating that O_{B-L} was almost completely consumed.

This designed H_2-TPR experiment not only provides direct evidence of the migration of O_{B-L}, but also confirms that the migration rate of O_{B-L} within CeO_2 under 600 °C is slow (lower than 0.0061 μmol/g per s).

In order to understand and explain the difference in catalytic stability between CeO_2 and the doped $Ce_{1-x}Y_xO_{2-\delta}$ catalyst samples, another designed H_2-TPR experiment was performed to compare the consumption of O_{S-L} of CeO_2 and $Ce_{0.75}Y_{0.25}O_{2-\delta}$ treated at 450 °C with 10 vol% H_2/Ar for 1 and 2 h.

H_2-TPR profiles of CeO_2, $Ce_{0.75}Y_{0.25}O_{2-\delta}$, and the treated samples are displayed in Fig. 8. It was found that the H_2 consumption peaks of both CeO_2 and $Ce_{0.75}Y_{0.25}O_{2-\delta}$ decreased with increasing treatment time. Besides, the reduction peaks of O_{S-L} were shifted towards a higher temperature, which could be attributed to the preferentially consumption of the most reactive and readily available lattice oxygen within samples as the results of Fig. S8. Comparing CeO_2 and $Ce_{0.75}Y_{0.25}O_{2-\delta}$ treated for 2 h, the reduction peak of the former was far smaller than the latter one. Moreover, the reduction peak of O_{B-L} in the treated CeO_2 samples moved towards lower temperature with the increase in treatment time with respect to untreated CeO_2, an observation which might be related to the migration of O_{B-L}.

The corresponding data obtained from this designed H_2-TPR experiment are summarized in Table 4. It is clear that the H_2 consumption peaks of the treated $Ce_{0.75}Y_{0.25}O_{2-\delta}$ were far larger than
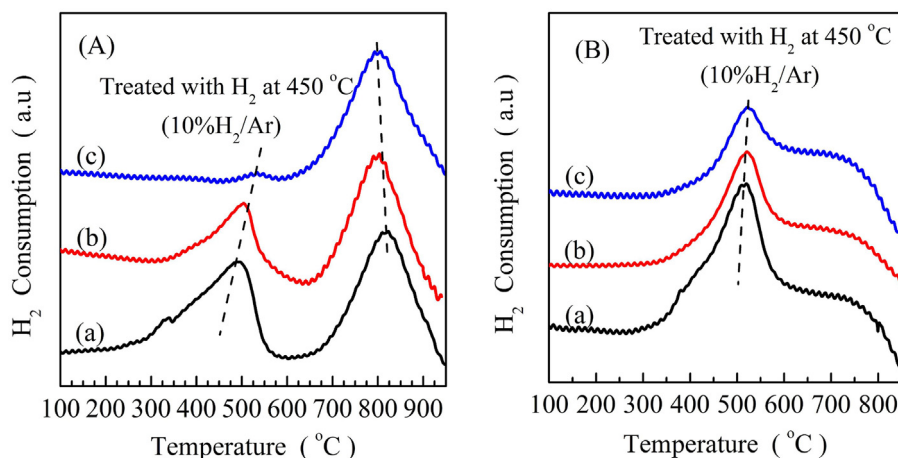
Fig. 8. Designed H_2-TPR profiles of (A) CeO_2 and (B) $Ce_{0.75}Y_{0.25}O_{2-\delta}$ treated with 10% H_2/Ar under 450 °C for different time (a) 0 h, (b) 1 h and (c) 2 h.

Table 5
Relative contents of surface lattice oxygen (O_{S-L}) and Ce^{3+} within $Ce_{0.75}Y_{0.25}O_{2-\delta}$ and $Ce_{0.75}Y_{0.25}O_{2-\delta}$ after time-on-stream test for different time.

Samples	Relative content of O_{S-L} (%) [a]	Relative content of Ce^{3+} (%) [b]
$Ce_{0.75}Y_{0.25}O_{2-\delta}$ (0) [c]	100	5.5
$Ce_{0.75}Y_{0.25}O_{2-\delta}$ (0.5) [c]	97	6.4
$Ce_{0.75}Y_{0.25}O_{2-\delta}$ (1.0) [c]	81	10.7
$Ce_{0.75}Y_{0.25}O_{2-\delta}$ (1.5) [c]	80	11.0
$Ce_{0.75}Y_{0.25}O_{2-\delta}$ (2.0) [c]	73	23.2
$Ce_{0.75}Y_{0.25}O_{2-\delta}$ (10.0) [c]	35	33.1
$Ce_{0.75}Y_{0.25}O_{2-\delta}$ (20) [c]	14	50.9

[a] The relative content of surface lattice oxygen (O_{S-L}) was calculated according to O1s spectra of $Ce_{0.75}Y_{0.25}O_{2-\delta}$ and $Ce_{0.75}Y_{0.25}O_{2-\delta}$ after time-on-stream test for different time, and the O_{S-L} relative content of fresh $Ce_{0.75}Y_{0.25}O_{2-\delta}$ was assigned to 100%.

[b] The relative content of Ce^{3+} was calculated according to the equations of (5), (6) and (7) based on Ce 3d spectra of $Ce_{0.75}Y_{0.25}O_{2-\delta}$ after time-on-stream test for various time.

[c] Reaction time of time-on-stream test in the brackets, and spent $Ce_{0.75}Y_{0.25}O_{2-\delta}$ after time-on-stream test for 20 h.

those of the treated CeO_2; this is closely associated with the fact that the migration rate of O_{B-L} within the former is faster than that of the latter. Herein, we assumed the H_2 consumption rate of O_{S-L} of CeO_2 and $Ce_{0.75}Y_{0.25}O_{2-\delta}$ to be the same. It can be deduced that the migration rate of O_{B-L} of $Ce_{0.75}Y_{0.25}O_{2-\delta}$ at 450 °C is larger than 0.0132 μmol/g per s, which is more than 2.1-fold the migration rate of O_{B-L} of CeO_2 at 600 °C.

3.3.3. XPS analysis

In order to further demonstrate the migration of O_{B-L} during the decomposition of CH_3SH, XPS was used to characterize $Ce_{0.75}Y_{0.25}O_{2-\delta}$ and $Ce_{0.75}Y_{0.25}O_{2-\delta}$ after the time-on-stream test for different time periods.

O1s and Ce3d core-level XPS spectra of $Ce_{0.75}Y_{0.25}O_{2-\delta}$ and $Ce_{0.75}Y_{0.25}O_{2-\delta}$ after time-on −stream test for different time are provided in Fig. 9, and the corresponding relative contents of O_{S-L} and Ce^{3+} are summarized in Table 5. As shown in Fig. 9A, there was a decrease in the photoelectron peak (529 eV) assigned to O_{S-L} with increasing reaction time, whereas no significant change was detected in the photoelectron peak of O_{S-A} with increasing reaction time. This may be explained as follows: on the one hand, O_{S-L} is able to participate in the catalytic decomposition of CH_3SH; on the other, O_{S-A} is not involved in the decomposition of CH_3SH.

As can be seen from Table 5, the relative contents of O_{S-L} within $Ce_{0.75}Y_{0.25}O_{2-\delta}$ after time-on-stream test for 1 and 1.5 h were 81% and 80%, respectively, thus implying that the relative content of

O_{S-L} is maintained relatively stable. This provides direct proof of the migration of O_{B-L} under the real reaction conditions. As displayed in Fig. 9B, two photoelectron peaks (located at 883.7 and 902.0 eV), belonging to the contribution of Ce^{3+} species, increased with increasing reaction time, thus indicating that more Ce^{4+} species were reduced into Ce^{3+} via the consumption of O_{S-L}.

For comparison purposes, the relative contents of O_{S-L} and Ce^{3+} within CeO_2 and $Ce_{0.75}Y_{0.25}O_{2-\delta}$ after the time-on-stream test for various time period are shown in Fig. 10. The decreased degree of the relative contents of O_{S-L} in $Ce_{0.75}Y_{0.25}O_{2-\delta}$ was smaller than that in CeO_2 and the relative content of Ce^{3+} within $Ce_{0.75}Y_{0.25}O_{2-\delta}$ was lower than that within CeO_2 after the time-on-stream test over the same time. This is likely due to the migration rate of O_{B-L} within $Ce_{0.75}Y_{0.25}O_{2-\delta}$ being faster than that of CeO_2.

3.3.4. Reaction products CO and CO_2 analyses

The concentration of the reaction products CO and CO_2 as a function of reaction time during the catalytic decomposition of CH_3SH over CeO_2 and $Ce_{0.75}Y_{0.25}O_{2-\delta}$ were investigated (Fig. S7). During the initial 3 h, the decrease in CO_2 concentration along with an increase in CO concentration was observed for both CeO_2 and $Ce_{0.75}Y_{0.25}O_{2-\delta}$ due to the consumption of O_{S-L} during CH_3SH decomposition to inhibit the oxidation of CO to CO_2. Moreover, the CO_2 concentration of $Ce_{0.75}Y_{0.25}O_{2-\delta}$ was higher than CeO_2 catalyst during the 2-h time-on-stream test, suggesting that a greater amount of the most reactive oxygen species and readily available lattice oxygen were produced within $Ce_{0.75}Y_{0.25}O_{2-\delta}$, as further confirmed by OSC experiments (Fig. S8). As the reaction time of the time-on-stream test approached 4–8 h, the CO concentration of $Ce_{0.75}Y_{0.25}O_{2-\delta}$ was comparable to that of CeO_2, and CO_2 was not observed. This might be due to the lack of a high enough O_{S-L} concentration to oxidize CO into CO_2. By further increasing the time of the time-on-stream test to 8 h, the CO concentration of $Ce_{0.75}Y_{0.25}O_{2-\delta}$ was universally higher than that of CeO_2, closely associated with the fact that the O_{B-L} of $Ce_{0.75}Y_{0.25}O_{2-\delta}$ rapidly migrated to replenish the consumed O_{S-L}.

Herein, the results of CO and CO_2 analysis provide direct proof to confirm that O_{S-L} is gradually consumed during the decomposition of CH_3SH and that the O_{B-L} of $Ce_{0.75}Y_{0.25}O_{2-\delta}$ rapidly migrates to replenish the depletion of O_{S-L} during the time-on-stream test.

3.3.5. OSC analysis

Yao et al. reported that the method of CO (or H_2) pulse injection could be used to measure the OSC of catalytic materials [71]; this has since been intensively adopted by several researchers to estimate the reactivity and mobility of oxygen in three-way catalysts
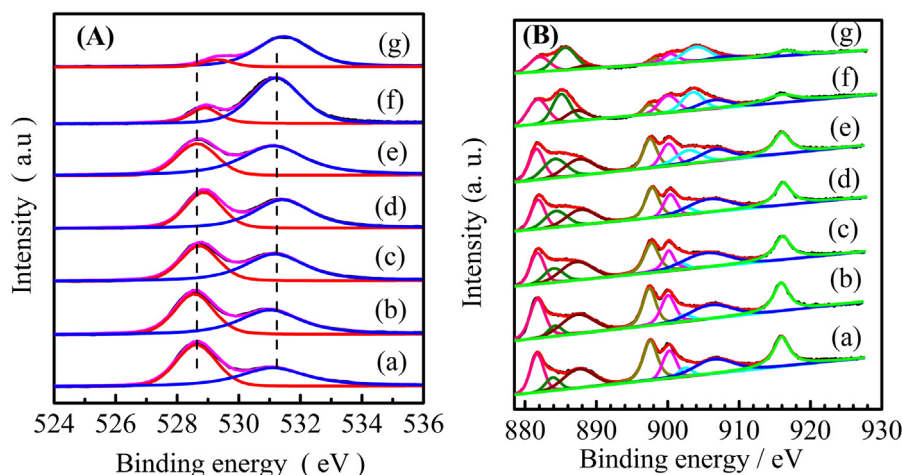
Fig. 9. (A) O1s and (B) Ce3d core level XP spectra of $Ce_{0.75}Y_{0.25}O_{2-\delta}$ and $Ce_{0.75}Y_{0.25}O_{2-\delta}$ after time-on-stream test for different time: (a) fresh, (b) 0.5 h, (c) 1.0 h, (d) 1.5 h, (e) 2 h, (f) 10 h and (g) spent.

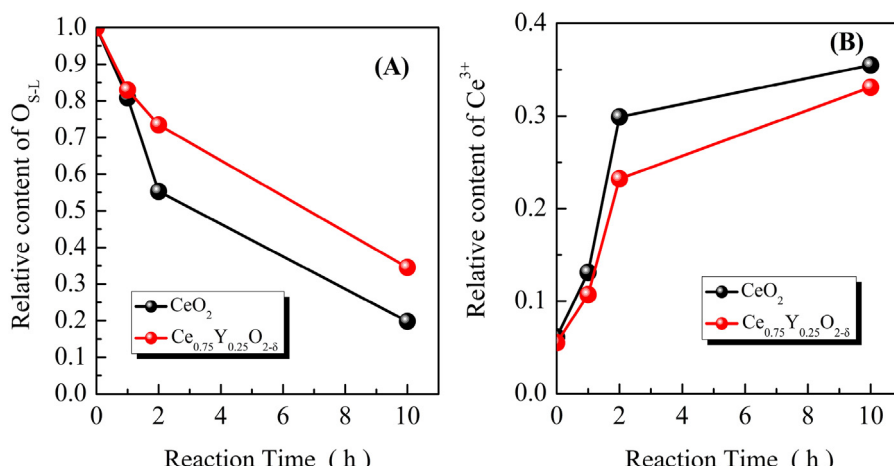**Fig. 10.** Relative contents of (A) surface lattice oxygen (O_{S-L}) and (B) Ce^{3+} within $Ce_{0.75}Y_{0.25}O_{2-\delta}$ and CeO_2 as a function of reaction time of time-on-stream test.

[72–75]. In general, the amount of the first CO (or H_2) uptake was designated as the OSC associated with the most reactive oxygen species and the most readily available lattice oxygen, and the total or maximum amount of CO (or H_2) uptake under the experiment conditions was nominated as the oxygen storage capacity complete (OSCC).

A CO pulse experiment was performed to investigate the OSC and the most reactive and readily available lattice oxygen within CeO_2 and $Ce_{0.75}Y_{0.25}O_{2-\delta}$ (Fig. S8). The quantitative data on the OSC and OSCC for CeO_2 and $Ce_{0.75}Y_{0.25}O_{2-\delta}$ samples were shown in Table S2. The greatest amount of CO was consumed over $Ce_{0.75}Y_{0.25}O_{2-\delta}$ for each CO pulse, and the greatest amount of CO_2 was produced at the same time. The OSC of $Ce_{0.75}Y_{0.25}O_{2-\delta}$ was higher than that of CeO_2 as shown in Table S2, indicating that there is a greater amount of the most reactive and readily available oxygen species within $Ce_{0.75}Y_{0.25}O_{2-\delta}$ than in CeO_2. These oxygen species are beneficial to the oxidization of CO, in agreement with the product analysis results showing that more CO_2 was formed over $Ce_{0.75}Y_{0.25}O_{2-\delta}$ during the first several hours.

The greater amount of OSCC within $Ce_{0.75}Y_{0.25}O_{2-\delta}$ was related to the greater amount of available oxygen species obtained from the experiment conditions. Thus, the CO pulse experiment results provide an indirect proof that the migration rate of O_{B-L} over $Ce_{0.75}Y_{0.25}O_{2-\delta}$ is superior to CeO_2.

3.4. The influencing factors of bulk lattice oxygen migration

In Sections 3.2 and 3.3, it was documented that $Ce_{0.75}Y_{0.25}O_{2-\delta}$ exhibits comparable catalytic activity and better stability in the decomposition of CH_3SH compared to CeO_2. The excellent stability of $Ce_{0.75}Y_{0.25}O_{2-\delta}$ is attributed to the rapid migration of O_{B-L}. Therefore, the factors that would influence the migration rate of O_{B-L} are investigated and discussed below.

The physicochemical properties (BET specific surface area, pore volume, crystal size, and lattice parameters) of CeO_2 and $Ce_{0.75}Y_{0.25}O_{2-\delta}$ are summarized in Table S1. The crystal size of $Ce_{0.75}Y_{0.25}O_{2-\delta}$ (6.35 nm) was far smaller than that of CeO_2 (10.43 nm), likely due to the fact that the addition of Y within $Ce_{0.75}Y_{0.25}O_{2-\delta}$ would effectively suppress crystal growth [48]. Generally, smaller crystal sizes are beneficial to the promotion of migration of O_{B-L} from the bulk to the surface of the particle due to the shorter migration distance. Therefore, the smaller particle size of $Ce_{0.75}Y_{0.25}O_{2-\delta}$ compared with that of CeO_2 is conducive to the migration of O_{B-L} to its surface to maintain the concentration of O_{S-L}, thereby improving its stability.

Furthermore, the lattice parameter of $Ce_{0.75}Y_{0.25}O_{2-\delta}$ (5.414 Å) is larger than that of CeO_2 (5.410 Å) due to the incorporation of the larger Y^{3+} ion (1.03 Å) into the lattice of CeO_2 [76]. Generally, the change in lattice parameters originating from the insertion of other ions into the lattice of CeO_2 would result in the formation of lattice

defects and/or lattice distortion, thereby improving the mobility of O_{B-L} [77]. It is well-documented that the insertion of aliovalent (e.g., La^{3+}, Sm^{3+}, $Eu^{2+/3+}$, Gd^{3+}) cations into the cubic fluorite structure of CeO_2 will lead to the generation of oxygen vacancy defects to maintain an electrostatic balance [78–80]. Raman characterization is a general and effective route to obtain deep insights into the formation of oxygen vacancy defects within cerium-based materials. Therefore, CeO_2 and $Ce_{0.75}Y_{0.25}O_{2-\delta}$ were characterized by Raman spectroscopy to investigate and demonstrate the presence of oxygen vacancy defects within them (Fig. S9). An intense peak located at approximately 465 cm^{-1}, attributed to the F_{2g} vibration mode of the oxygen atom (O) surrounded by Ce^{4+} ion [81,82], was detected in the spectra of both CeO_2 and $Ce_{0.75}Y_{0.25}O_{2-\delta}$, thus implying that the fluorite-type structure of CeO_2 is maintained in $Ce_{0.75}Y_{0.25}O_{2-\delta}$. Two Raman peaks centered at approximately 560 and 610 cm^{-1} were obviously expressed in the spectrum of $Ce_{0.75}Y_{0.25}O_{2-\delta}$, but not for CeO_2 (Fig. S9B). The former band (560 cm^{-1}) was ascribed to the formation of extrinsic oxygen vacancy defects originating from the substitution of every two tetravalent Ce^{4+} ions by two trivalent Y^{3+} ions in order to maintain electrostatic charge neutrality in the CeO_2 lattice. The latter (610 cm^{-1}) was attributed to the presence of intrinsic oxygen vacancy defects arising from lattice expansion and/or distortion due to ionic radii disparity between Ce^{4+} and Y^{3+} [83–85]. According to Raman characterization, it can be concluded that the greater formation of oxygen vacancy defects within $Ce_{0.75}Y_{0.25}O_{2-\delta}$ will enhance the mobility of O_{B-L} [86], thus finally improving its catalytic stability.

4. Conclusion

A series of $Ce_{1-x}Y_xO_{2-\delta}$ (x = 0, 0.25, 0.50, 0.75, and 1.0) solid solutions were prepared, characterized, and tested using CH_3SH as a model reactant to investigate the relation between catalytic activity and surface lattice oxygen and that between catalytic stability and bulk lattice oxygen. Surface lattice oxygen, rather than adsorbed oxygen, plays a key role in model reactions over cerium-based oxygen carriers. The difference in catalytic activity between CeO_2 and Y-doped samples was attributed to the introduction of Y^{3+} ion into the lattice of CeO_2 causing loss of surface lattice oxygen. The more Y^{3+} ions incorporated into the lattice of CeO_2, the greater the amount of surface lattice oxygen lost, resulting in a decrease in catalytic activity. The improvement of catalytic stability is closely associated with the faster migration of bulk lattice oxygen, which participates in the decomposition of CH_3SH via its migration to replenish surface lattice oxygen. H_2-TPR, designed H_2-TPR, XPS, reaction products (CO and CO_2) analysis, and OSC provided direct and indirect evidences to confirm bulk lattice oxygen migration and that the migration rate of bulk lattice oxygen within $Ce_{0.75}Y_{0.25}O_{2-\delta}$ is faster (more than 2.1-fold) than within CeO_2.

Acknowledgements

Appendix A. Supplementary data

Supplementary data associated with this article can be found, in the online version, at doi:10.1016/j.apcatb.2017.06.053.

References

[1] C.T. Campbell, C.H.F. Peden, Science 309 (2005) 713–714.
[2] V. Ulricha, B. Morozb, I. Sineva, P. Pyriaev, V. Bukhtiyarov, W. Grünert, Appl. Catal. B Environ. 203 (2017) 572–581.
[3] J. Gong, D. Wang, J.H. Li, N. Currier, A. Yezerets, Appl. Catal. B Environ. 203 (2017) 936–945.
[4] A.S. Bobin, V.A. Sadykov, V.A. Rogov, N.V. Mezentseva, G.M. Alikina, E.M. Sadovskaya, T.S. Glazneva, N.N. Sazonova, M.Y. Smirnova, S.A. Veniaminov, C. Mirodatos, V. Galvita, G.B. Marin, Top. Catal. 56 (2013) 958–968.
[5] D. Pakhare, J. Spivey, Chem. Soc. Rev. 43 (2014) 7813–7837.
[6] B.C.H. Steele, A. Heinzel, Nature 414 (2001) 345–352.
[7] P. Yang, S.S. Yang, Z.N. Shi, Z.H. Meng, R.X. Zhou, Appl. Catal. B Environ. 162 (2015) 227–235.
[8] U. Menon, H. Poelman, V. Bliznuk, V.V. Galvita, D. Poelman, G.B. Marin, J. Catal. 295 (2012) 91–103.
[9] D.M. Gómez, J.M. Gaticaa, J.C. Hernández-Garrido, G.A. Cifredo, M. Montes, O. Sanz, J.M. Rebled, H. Vidal, Appl. Catal. B Environ. 144 (2014) 425–434.
[10] Q. Fu, H. Saltsburg, M. Flytzani-Stephanopoulos, Science 301 (2003) 935–938.
[11] C. Wen, Y. Zhu, Y. Ye, S. Zhang, F. Cheng, Y. Liu, P. Wang, F. Tao, ACS Nano 6 (2012) 9305–9313.
[12] V.V. Galvita, H. Poelman, V. Bliznuk, C. Detavernier, G.B. Marin, Ind. Eng. Chem. Res. 52 (2013) 8416–8426.
[13] K. Otsuka, Y. Wang, M. Nakamura, J. Catal. 183 (1999) 317–324.
[14] K. Otsuka, Y. Wang, E. Sunada, I. Yamanaka, J. Catal. 175 (1998) 152–160.
[15] X. Zhu, H. Wang, Y.G. Wei, K.Z. Li, X.M. Chen, J. Rare Earth 28 (2010) 907–913.
[16] H.H. Jeong, J.H. Kwak, G.Y. Han, K.J. Yoon, Int. J. Hydrogen Energy 36 (2011) 15221–15230.
[17] A. Murugan, A. Thursfield, I.S. Metcalfe, Energy Environ. Sci. 4 (2011) 4639.
[18] G. Voitic, V. Hacker, RSC Adv. 6 (2016) 98267.
[19] Z. Sarshar, F. Kleitzb, S. Kaliaguine, Energy Environ. Sci. 4 (2011) 4258.
[20] M. Rydén, M. Johansson, A. Lyngfelta, T. Mattisson, Energy Environ. Sci. 2 (2009) 970–981.
[21] A. Thursfield, A. Murugan, R. Franca, I.S. Metcalfe, Energy Environ. Sci. 5 (2009) 7421.
[22] S.W. Luo, L. L.Zeng, D.K. Xu, E. Chung, N. Deshpande, L. Qin, A. Majumder, T.L. Hsieh, A. Tong, Z.C. Sun, L.S. Fan, Energy Environ. Sci. 7 (2014) 4104.
[23] M. Meledina, S. Turner, V.V. Galvita, H. Poelman, G.B. Marin, G. Van Tendeloo, Nanoscale 7 (2015) 3196.
[24] C.L. Muhich, B.W. Evanko, K.C. Weston, P. Lichty, X. Liang, J. Martinek, C.B. Musgrave, A.W. Weimer, Science 341 (2013) 540–542.
[25] B. Moghtaderi, Energy Fuels 26 (2012) 15–40.
[26] W.C. Chueh, C. Falter, M. Abbott, D. Scipio, P. Furler, S.M. Haile, A. Steinfeld, Science 330 (2010).
[27] S. Abanades, A. Legal, A. Cordier, G. Peraudeau, G. Flamant, A. Julbe, J. Mater Sci. 45 (2010).
[28] H. Kaneko, S. Taku, Y. Naganuma, T. Ishihara, N. Hasegawa, Y. Tamaura, J. Solar Energy Eng. 132 (2010), 0212021-4.
[29] S. Abanades, G. Flamant, Sol. Energy 80 (2006) 1611–1623.
[30] M. Fathi, E. Bjorgum, T. Viig, O.A. Rokstad, Catal. Today 63 (2000) 489–497.
[31] K.H. Hofstad, J.H.B.J. Hoebink, A. Holmen, G.B. Marin, Catal. Today 40 (1998) 157.
[32] V.A. Sadykov, T.G. Kuznetsova, G.M. Alikina, Y.V. Frolova, A.I. Lukashevich, Y.V. Potapova, V.S. Muzykantov, V.A. Rogov, V.V. Kriventsov, D.I. Kochubei, E.M. Moroz, D.I. Zyuzin, V.I. Zaikovskii, V.N. Kolomiichuk, E.A. Paukshtis, E.B. Burgina, V.V. Zyryanov, N.F. Uvarov, S. Neophytides, E. Kemnitz, Catal. Today 93–95 (2004) 45–53.
[33] X.P. Dai, R.J. Li, C.C. Yu, Z.P. Hao, J. Phys. Chem. B 110 (2006) 22525–22531.
[34] X.P. Dai, Q. Wu, R.J. Li, C.C. Yu, Z.P. Hao, J. Phys. Chem. B 110 (2006) 25856–25862.
[35] M. Rydén, A. Lyngfelt, T. Mattisson, Energy Fuels 24 (2008) 2585–2597.
[36] Z.H. Gu, K.Z. Li, S. Qing, X. Zhu, Y.G. Wei, Y.T. Li, H. Wang, RSC Adv. 4 (2014) 47191.
[37] C. Cammarano, E. Huguet, R. Cadours, C. Leroi, B. Coq, V. Hulea, Appl. Catal. B Environ. 156–157 (2014) 128–133.
[38] E. Huguet, B. Coq, R. Durand, C. Leroi, R. Cadours, V. Hulea, Appl. Catal. B Environ. 134–135 (2016) 344–348.
[39] S.Y. Jung, J.M. Moon, S.C. Lee, S.C. Paik, K.S. Park, J.C. Kim, Adsorpt 20 (2014) 341–348.
[40] S.H. Wang, Y. Fan, J. Chem. Eng. 256 (2014) 14–22.
[41] N. Laosiripojana, S. Assabumrungrat, Appl. Catal. B Environ. 102 (2011) 267–275.
[42] M. Flytzani-Stephanopoulos, M. Sakbodin, Z. Wang, Science 312 (2006) 1508–1510.
[43] M. Behl, J. Yeom, Q. Lineberry, P. Jain, M. Shannon, Nat. Nanotechnol. 7 (2012) 810–815.
[44] D.D. He, G.P. Wan, H.S. Hao, D.K. Chen, J.C. Lu, L. Zhang, F. Liu, L.P. Zhong, S.F. He, Y.M. Luo, Chem. Eng. J. 289 (2016) 161–169.
[45] D.D. He, H.S. Hao, D.K. Chen, J.C. Lu, L.P. Zhong, R. Chen, F. Liu, G.P. Wan, S.F. He, Y.M. Luo, J. Environ. Chem. Eng. 4 (2016) 311–318.
[46] D.D. He, H.S. Hao, D.K. Chen, J.P. Liu, J. Yu, J.C. Lu, F. Liu, G.P. Wan, S.F. He, Y.M. Luo, Catal. Today 281 (2017) 559–565.
[47] D.D. He, D.K. Chen, H.S. Hao, J. Yu, J.P. Liu, J.C. Lu, F. Liu, G.P. Wan, S.F. He, Y.M. Luo, Appl. Surf. Sci. 390 (2016) 959–967.
[48] M. Fabián, B. Antić, V. Girman, M. Vučinić-Vasić, A. Kremenović, S. Suzuki, H. Hahn, V. Šepelák, J. Solid State Chem. 230 (2015) 42–48.
[49] Y.M. Luo, Z.Y. Hou, J. Gao, D.F. Jin, X.M. Zheng, Mater. Sci. Eng. B 140 (2007) 123–127.
[50] X.L. Sang, L.Y. Zhang, H. Wang, D.D. He, L. Deng, S. Huang, J. Wang, Y.M. Luo, Powder Technol. 253 (2014) 590–595.

[51] Y.P. Fu, S.H. Chen, J.J. Huang, Int. J. Hydrogen Energy 35 (2010) 745–752.
[52] K.C. Anjaneya, G.P. Nayaka, J. Manjanna, G. Govindaraj, K.N. Ganesha, J. Alloys Compd. 585 (2014) 594–601.
[53] T. Vinodkumar, B.G. Rao, B.M. Reddy, Catal. Today 253 (2015) 57–64.
[54] D. Yang, L. Wang, Y.Z. Sun, K.B. Zhou, J. Phys. Chem. C 114 (2010) 8926–8932.
[55] Z. Wang, Z.P. Qu, X. Quan, Z. Li, H. Wang, R. Fan, Appl. Catal. B Environ. 134–135 (2013) 153–166.
[56] J. Hierso, O. Sel, A. Ringuede, C. Laberty-Robert, L. Bianchi, D. Grosso, C. Sanchez, Chem. Mater. 21 (2009) 2184.
[57] J. Fan, X.D. Wu, X.D. Wu, Q. Liang, R. Ran, D. Weng, Appl. Catal. B Environ. 81 (2008) 38–48.
[58] W. Fang, C. Pirez, S. Paul, M. Capron, H. Jobic, F. Dumeignil, L. Jalowiecki-Duhamel, ChemCatChem 5 (2013) 2207–2216.
[59] Y.C. Lee, K.D. Li, C.H. Lu, J.H. Shen, L.G. Teoh, G.W. Chiang, J. Electron. Mater. 42 (2013).
[60] M. Fernandez-Garcia, A. Martinez-Arias, A. Iglesias-Juez, C. Belver, A.B. Hungria, J.C. Conesa, J. Soria, J. Catal. 194 (2000) 385.
[61] P. Vidmar, P. Fornasiero, J. Kaspar, G. Gubitosa, M. Graziani, J. Catal. 171 (1997) 160.
[62] W. Deng, Q.G. Dai, Y.J. Lao, B.B. Shi, X.Y. Wang, Appl. Catal. B Environ. 181 (2016) 848–861.
[63] Q. Ye, R.P. Wang, B.Q. Xu, Acta Phys. –Chim. Sin. 22 (1) (2006) 33–37.
[64] A.E.C. Palmqvist, M. Wirde, U. Gelius, M. Muhammed, NanoStruct. Mater. 11 (8) (1999) 995.
[65] C.T. Campbell, C.H.F. Peden, Science 309 (2005) 713–714.
[66] G. Balducci, M.S. Islam, P. Fornasiero, M. Graziani, Chem. Mater. 12 (2000) 677–681.
[67] J. Li, Y.X. Han, Y.H. Zhu, R.X. Zhou, Appl. Catal. B Environ. 108–109 (2011) 72–80.
[68] Y.C. Wei, J. Liu, Z. Zhao, A.J. Duan, G.Y. Jiang, J. Catal. 287 (2012) 13–29.
[69] Y.C. Huang, B. Long, M.N. Tang, Z.B. Rui, M.S. Balogun, Y.X. Tong, Appl. Catal. B Environ 181 (2016) 779–787.
[70] M. Rumruangwong, S. Wongkasemjit, Appl. Organomet. Chem. 20 (2006) 615.
[71] H.C. Yao, Y.F. Yu Yao, J. Catal. 86 (1984) 254.
[72] P.S. Lambrou, C.N. Costa, S.Y. Christou, A.M. Efstathiou, Appl. Catal. B Environ. 54 (2004) 237–250.
[73] G. Li, B. Zhao, Q. Wang, R. Zhou, Appl. Catal. B Environ. 97 (2010) 41–48.
[74] P.S. Lambrou, K. Polychronopoulou, K.C. Petallidou, A.M. Efstathiou, Appl. Catal. B Environ. (2016).
[75] J. Li, X.F. Liu, W.C. Zhan, Y. Guo, Y.L. Guo, G.Z. Lu, Catal. Sci. Technol. 6 (2016) 897–907.
[76] J.G. Li, T. Ikegami, Y.R. Wang, T. Mori, J. Solid State Chem. 168 (2002) 52–59.
[77] Y.N. Zheng, K.Z. Li, H. Wang, D. Tian, Y.H. Wang, X. Zhu, Y.G. Wei, M. Zheng, Y.M. Luo, Appl. Catal. B Environ. 202 (2017) 51–63.
[78] L. Li, F. Chen, J.Q. Lu, M.F. Luo, J. Phys. Chem. A 115 (27) (2011) 7972–7977.
[79] C. Sun, H. Li, L. Chen, Energy Environ. Sci. 5 (2012) 8475.
[80] C. Levy, C. Guizard, A. Julbe, J. Am. Ceram. Soc. 90 (2007) 942.
[81] D. Harshini, D.H. Lee, J. Jeong, Y. Kim, S.W. Nam, H.C. Ham, J.H. Han, T.H. Lim, C.W. Yoon, Appl. Catal. B Environ. 148–149 (2014) 415–423.
[82] L. Ma, D. Wang, J. Li, B. Bai, L. Fu, Y. Li, Appl. Catal. B Environ. 148 (2014) 36–43.
[83] D.N. Durgasri, T. Vinodkumar, B.M. Reddy, J. Chem. Sci. 126 (2014) 429–435.
[84] D. Naga Durgasri, T. Vinodkumar, P. Sudarsanam, B.M. Reddy, Catal. Lett. 144 (2014) 971–979.
[85] W. Lee, S.Y. Chen, Y.S. Chen, C.L. Dong, H.J. Lin, C.T. Chen, A. Gloter, J. Phys. Chem. C 118 (2014) 26359–26367.
[86] X.W. Liu, K.B. Zhou, L. Wang, B.Y. Wang, Y.D. Li, J. Am. Chem. Soc. 131 (2009) 3140.